The effect of abdominal wall morphology on ultrasonic pulse distortion. Part II. Simulations

T. Douglas Mast
Applied Research Laboratory, The Pennsylvania State University, University Park, Pennsylvania 16802

Laura M. Hinkelman[a)]
Department of Electrical Engineering, University of Rochester, Rochester, New York 14627

Michael J. Orr
Department of Electrical Engineering, University of Rochester, Rochester, New York 14627

Robert C. Waag
Departments of Electrical Engineering and Radiology, University of Rochester, Rochester, New York 14627

(Received 14 December 1997; revised 13 July 1998; accepted 17 August 1998)

Wavefront propagation through the abdominal wall was simulated using a finite-difference time-domain implementation of the linearized wave propagation equations for a lossless, inhomogeneous, two-dimensional fluid as well as a simplified straight-ray model for a two-dimensional absorbing medium. Scanned images of six human abdominal wall cross sections provided the data for the propagation media in the simulations. The images were mapped into regions of fat, muscle, and connective tissue, each of which was assigned uniform sound speed, density, and absorption values. Propagation was simulated through each whole specimen as well as through each fat layer and muscle layer individually. Wavefronts computed by the finite-difference method contained arrival time, energy level, and wave shape distortion similar to that in measurements. Straight-ray simulations produced arrival time fluctuations similar to measurements but produced much smaller energy level fluctuations. These simulations confirm that both fat and muscle produce significant wavefront distortion and that distortion produced by fat sections differs from that produced by muscle sections. Spatial correlation of distortion with tissue composition suggests that most major arrival time fluctuations are caused by propagation through large-scale inhomogeneities such as fatty regions within muscle layers, while most amplitude and waveform variations are the result of scattering from smaller inhomogeneities such as septa within the subcutaneous fat. Additional finite-difference simulations performed using uniform-layer models of the abdominal wall indicate that wavefront distortion is primarily caused by tissue structures and inhomogeneities rather than by refraction at layer interfaces or by variations in layer thicknesses.
 [S0001-4966(98)06011-1]

PACS numbers: 43.80.Cs, 43.80.Vj, 43.20.Fn, 43.58.Ta [FD]

INTRODUCTION

Wavefront distortion is considered to be a significant obstacle to improved ultrasonic image quality. However, little is known about its actual cause. Some direct measurements have been made to characterize the distortion produced by various tissues.[1–6] These measurements have yielded parameters describing wavefront distortion from these tissues, but have provided limited insight into the actual causes of the distortion.

Because basic knowledge about the physical causes of wavefront distortion is lacking, researchers have relied on a variety of assumptions to develop wavefront distortion correction algorithms. Several early algorithms were based on the assumption that wavefront distortion produced by propagation through soft tissue consisted solely of phase aberrations that could be modeled as the result of a phase screen in the measurement aperture.[7–10] This model of wavefront distortion was supported by the results of an experimental study[11] in which poor ultrasonic image quality was found to correlate with the presence of phase errors while little amplitude distortion was detected. However, later studies indicated that amplitude and wave shape distortion occur as well.[2,4–6,12] To accommodate this finding, distortion has been modeled as the result of a phase screen some distance from the aperture[13–15] or as a phase screen and an amplitude screen at the aperture.[16,17]

A greater knowledge of the mechanisms that cause wavefront distortion would improve understanding of what is required for successful distortion compensation. Several investigators have attempted to improve this understanding by calculating distortion using ray-tracing or other simplified models.[18–22] However, these simulations have also been based on simple assumptions about the structure of the body wall and the causes of wavefront distortion. For example, one study[18] employed measured scattering from liver tissue and model random media to estimate wavefront distortion using a weak scattering approximation. Ødegaard[19,20] used a ray-tracing technique that was limited to refraction effects,

[a)]Current address: Department of Meteorology, The Pennsylvania State University, University Park, Pennsylvania 16802.

and assumed a very simple tissue geometry. Manry,[21] in a model of propagation through breast tissue, applied a finite-difference time-domain method to a similarly simple tissue model so that refraction dominated the effects observed. Berkhoff *et al.*,[22] in computations employing conjugate gradient techniques to evaluate the Rayleigh integral, concerned themselves only with the effect of propagation through an irregular interface. In other computations from the same group,[15] tissue has been modeled as succession of random phase screens.

In a recent study,[23,24] a full-wave simulation technique was applied to tissue models based on images of actual human abdominal wall cross sections. Results of that study demonstrated that this finite-difference time-domain simulation produced arrival time, energy level, and wave shape distortion similar to that measured for large abdominal wall specimens. The study also showed that amplitude distortion produced by the abdominal wall can be described as the result of strong scattering.

The purpose of the present study is to use the simulation technique described in Ref. 23 to examine the causes of ultrasonic wavefront distortion in the abdominal wall. In particular, questions concerning the relative contributions of the fat and muscle layers to distortion and the importance of the interface between these layers are investigated. Quantitative correlation methods are employed to relate specific tissue structures to computed wavefront distortion features. Distortion predicted by finite-difference simulations is also compared with results of simulations employing more idealized models of ultrasound-tissue interactions. The simulation results are qualitatively compared with experimental results reported in the companion paper.[25]

I. METHOD

Propagation of ultrasonic pulses through the fat and muscle layers of the abdominal wall was simulated in two dimensions using the tissue modeling technique and the lossless finite-difference time-domain (FDTD) algorithm described in Ref. 23. The six tissue maps of abdominal wall cross sections employed in the previous study were again used as input to the FDTD program. However, in this case the tissue maps were also separated into fat and muscle layers along the center of the septum dividing the layers, and the propagation of an ultrasonic pulse through each layer was calculated individually.

The tissue maps were made by processing scanned images of abdominal wall cross sections which had been stained to distinguish tissue types according to the procedure described in Ref. 26. Regions of the images containing connective tissue (e.g., skin, tendon, and septa), muscle, and fat were color coded. Density and sound speed arrays for the finite-difference computation, as well as absorption arrays used in the straight-ray computations discussed below, were created from these images by mapping the various colors to representative density and sound speed values obtained from the literature for each tissue type. The values employed are the same as those reported in Ref. 23, and are shown in Table I for reference. The 12 tissue maps employed are shown in Fig. 1.

TABLE I. Sound speed, density, and attenuation parameters employed in finite-difference and straight-ray simulations. Attenuation values shown are those appropriate for a center frequency of 3.75 MHz. These values were compiled in Ref. 23.

Medium	Sound speed (mm/μs)	Density (g/cm^3)	Attenuation (dB/cm)
Water	1.524	0.993	0.02
Fat	1.478	0.950	1.8
Muscle	1.547	1.050	4.1
Skin/CT	1.613	1.120	5.9

The general appearance of the cross sections is consistent with descriptions from standard anatomical texts[27–29] and the human specimens shown in Ref. 25. The fat sections are composed primarily of subcutaneous fat lobules separated by thin connective tissue membranes (septa). Inhomogeneities, mainly consisting of fat, are present in all the muscle sections. Boundaries between muscle, fat, skin, and water (exterior to the specimen) in this figure are not entirely smooth. The roughness seen in these boundaries is substantially greater than that occurring *in vivo* or in measurements[25] because the cross sections were fixed in formalin while still stiff from being frozen for the cutting procedure.

Specific anatomical features can also be observed in each of the tissue maps in Fig. 1. Cross section 75hi (a) shows a cross section of the rectus muscle cut perpendicular to the midline of the body. The thick connective tissue to the right is the linea alba. Cross section 77ba (b) shows the rectus muscle on the right. At the left side of the cross section, muscle layers shown are the external and internal obliques, cut diagonally to the cross section, as well as the transversus abdominus, cut parallel to the cross section. Cross section 87de (c) is cut along the rectus muscle parallel to the midline of the body. A fibrous connection, or aponeurosis, is shown, but is mostly composed of fat.[25] A fatty region is evident within the muscle layer to the left. The skin is also thicker than in the other cross sections. Cross section 102gh (d) is cut perpendicular to the rectus muscle. Blood vessels are evident both within the subcutaneous fat and in a fatty region that occurs within the thin muscle section. Both cross sections 120de (e) and 120fe (f) are cut along the rectus muscle from the same abdominal wall specimen. An aponeurosis, which does not extend through the entire muscle layer in the vertical direction,[27] is evident in both sections.

The simulation parameters were chosen to emulate the measurement configuration described in Refs. 2 and 25. Propagation of a plane-wave pulse through each layer was computed. The pulse had a center frequency of 3.75 MHz and a -6-dB bandwidth of 1.6 MHz. The waveforms exiting each cross section were recorded at a sampling rate of 225 MHz for 7.3 μs by 128 simulated receivers 0.72 mm in width placed about 8 mm from the skin surface.

A one-dimensional version of the reference waveform method[23] was used to calculate the arrival time of the pulse at each receiving position in the simulation data. The arrival time fluctuations across the receiving aperture caused by each whole or layer cross section were calculated by sub-

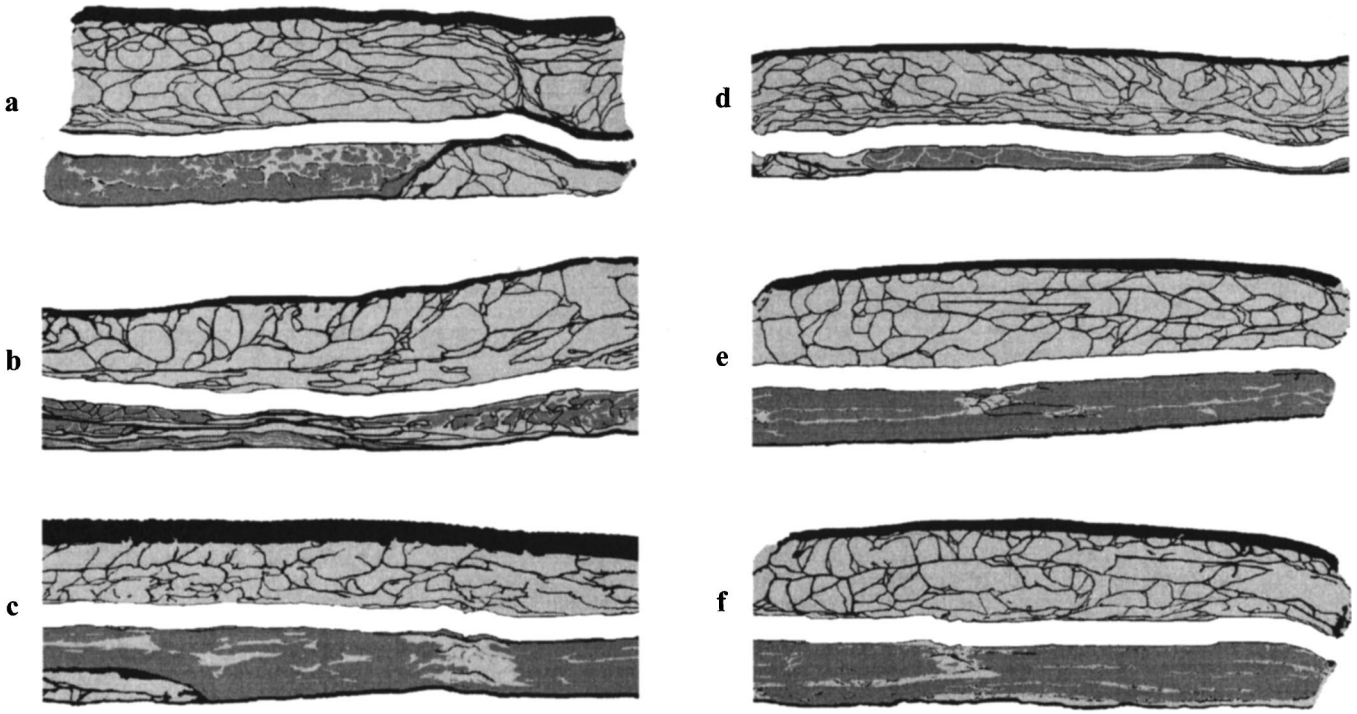

FIG. 1. Muscle-layer and fat-layer tissue maps employed in simulations. Black denotes connective tissue, dark gray denotes muscle, and light gray denotes fat. The fat layers (above) and the muscle layers (below) are obtained in each case from the whole-specimen maps shown in Ref. 23. The actual width of each map shown is 110 mm. (a) Cross section 75hi. (b) Cross section 77ba. (c) Cross section 87de. (d) Cross section 102gh. (e) Cross section 120de. (f) Cross section 120fe.

tracting a linear fit from these calculated arrival times. This fit, when applied to the one-dimensional fluctuations, compensated for gross changes in tissue thickness in a manner similar to higher-order fits previously employed for two-dimensional fluctuations.[1,2,5,6,23] Energy level fluctuations in the wavefronts were calculated by summing the squared amplitudes of each waveform over a 2.4-μs window that isolated the main pulse, converting to decibel units, and subtracting the best linear fit from the resulting values. Variations in pulse shape across the aperture were evaluated using the waveform similarity factor.[13]

Insertion losses were also calculated from the finite-difference time-domain results. Water path results computed by the methods described above, using a constant sound speed of 1.524 mm/μs and a constant density of 0.993 g/cm^3, were used as reference amplitude values. Insertion loss values were then determined by comparing peak amplitudes of analytic envelopes for tissue-path and water-path signals for each simulated receiver. Since no explicit absorption was included in the finite-difference simulation, and since any numerical absorption due to finite-difference discretization appeared in both tissue- and water-path computations, the resulting attenuation was due only to effects of propagation through the inhomogeneous tissue.

Arrival time fluctuations, energy level fluctuations, and insertion loss were also computed for the modeled cross sections using the asymptotic technique described in Ref. 23. In this case, ultrasonic rays were assumed to pass directly through the tissue without deviation from their initial direction of propagation. The arrival time for rays spaced 0.0847 mm apart was calculated by summing the travel time along the path of propagation. Likewise, the relative energy level of each ray was computed by integrating the spatially dependent absorption coefficient from Table I along the ray paths. Arrival time and energy level surfaces were determined for the 128-element simulated aperture by averaging arrival times and energy levels for rays occurring within the span of each simulated element (eight or nine rays were averaged for each element). Arrival time and energy level fluctuations were then computed by subtracting the best linear fit from the results of each simulation. The output waveforms were assumed to be identically shaped (waveform similarity factor equal to 1) for the asymptotic straight-ray computation since no mechanism for wave-shape distortion was included in the model. Average bulk attenuation values were also computed for each whole and partial cross section as a function of position along the simulated aperture by integrating absorption values along each ray path. No water-path results were computed for the straight-ray method.

For each ray path employed in the straight-ray computations, the total propagation length within individual tissue types (including fat, muscle, connective tissue, and water) was determined by simple summation. These lengths were then normalized by the total propagation path to obtain the fractional contribution of each tissue type to each ray path. As with the arrival time and attenuation values, tissue fractions for each tissue type were averaged for rays occurring within the span of each element to obtain tissue-fraction curves.

For whole and sectioned maps and both straight-ray and finite-difference simulations, correlation coefficients between the arrival time and energy level curves and the tissue-

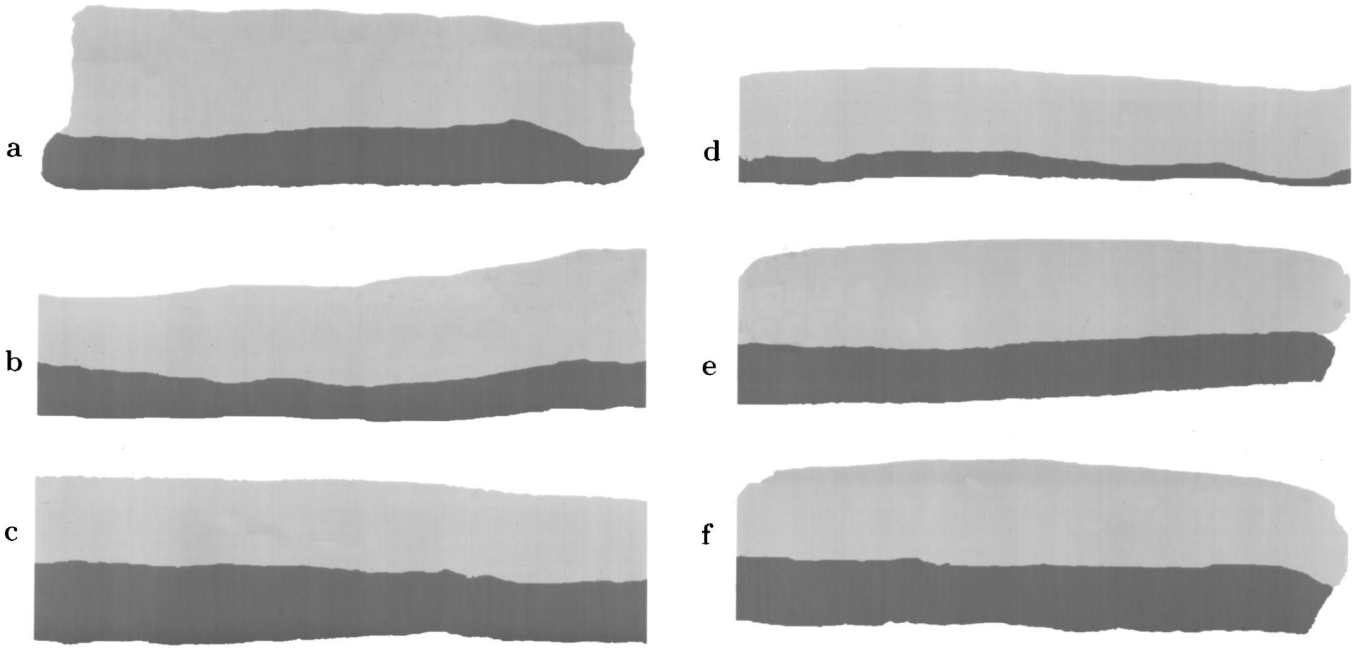

FIG. 2. Solid-layer tissue maps employed in simulations. Cross sections are mapped and ordered as in Fig. 1.

fraction curves were computed. In each case, the correlated curves were 128-point functions corresponding to the 128-element simulated aperture. In addition, arrival time fluctuation and energy level fluctuation curves were summed for the fat and muscle sections of all simulations for comparison with the whole-specimen results.

In order to evaluate the relative importance of tissue boundaries and layer-thickness variations in producing wavefront distortion, finite-difference and straight-ray simulations were also performed for tissue maps composed of uniform layers. These maps were obtained by altering the layers from Fig. 1 so that the upper layer contained only homogeneous fat and the lower layer contained only homogeneous muscle. The uniform-layer tissue maps are shown in Fig. 2. Data obtained using uniform-layer simulations were processed in the same manner as the data from the simulations employing full tissue structure.

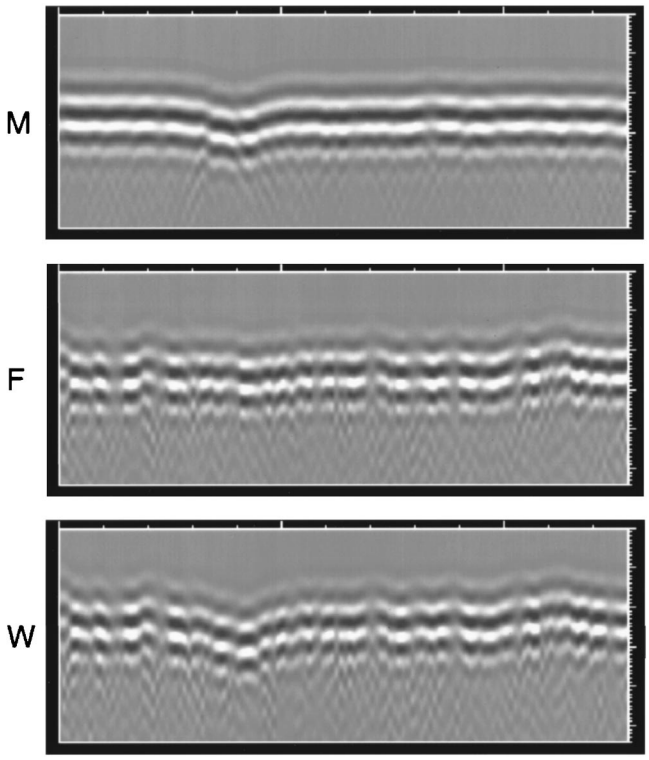

FIG. 3. Simulated waveforms for cross section 120fe (W) and its muscle (M) and fat (F) layers. Waveforms are shown on a linear gray scale with time as the vertical axis and element number as the horizontal axis. The temporal range shown is 2.3 μs for 128 elements.

II. RESULTS

Waveforms simulated by the finite-difference method for cross section 120fe are shown in Fig. 3. The waveforms appear similar to measured waveforms recorded for the same abdominal wall specimen,[23] and show several characteristics common to data from the cross sections studied here. Specifically, the muscle-layer wavefront shows substantial arrival time variation that is primarily associated with propagation through a large-scale inhomogeneity (in this case, a fatty aponeurosis), while energy level fluctuations and waveform variations are small. The fat-layer wavefront shows smaller-scale arrival time variations as well as waveform distortion and localized amplitude dropouts. The full-specimen wavefront roughly appears to be a combination of the two layer wavefronts, containing both the large-scale features of the muscle-layer wavefront and the smaller-scale aberrations of the fat-layer wavefront.

Arrival time and energy level distortion simulated using the finite-difference method for whole abdominal wall cross sections, muscle layers, and fat layers are graphically summarized in Figs. 4 and 5, respectively. Panel (f) of each figure shows distortion curves obtained from the waveforms shown in Fig. 3. Although Figs. 4 and 5 show individual variations in the relative contributions of tissue layers to

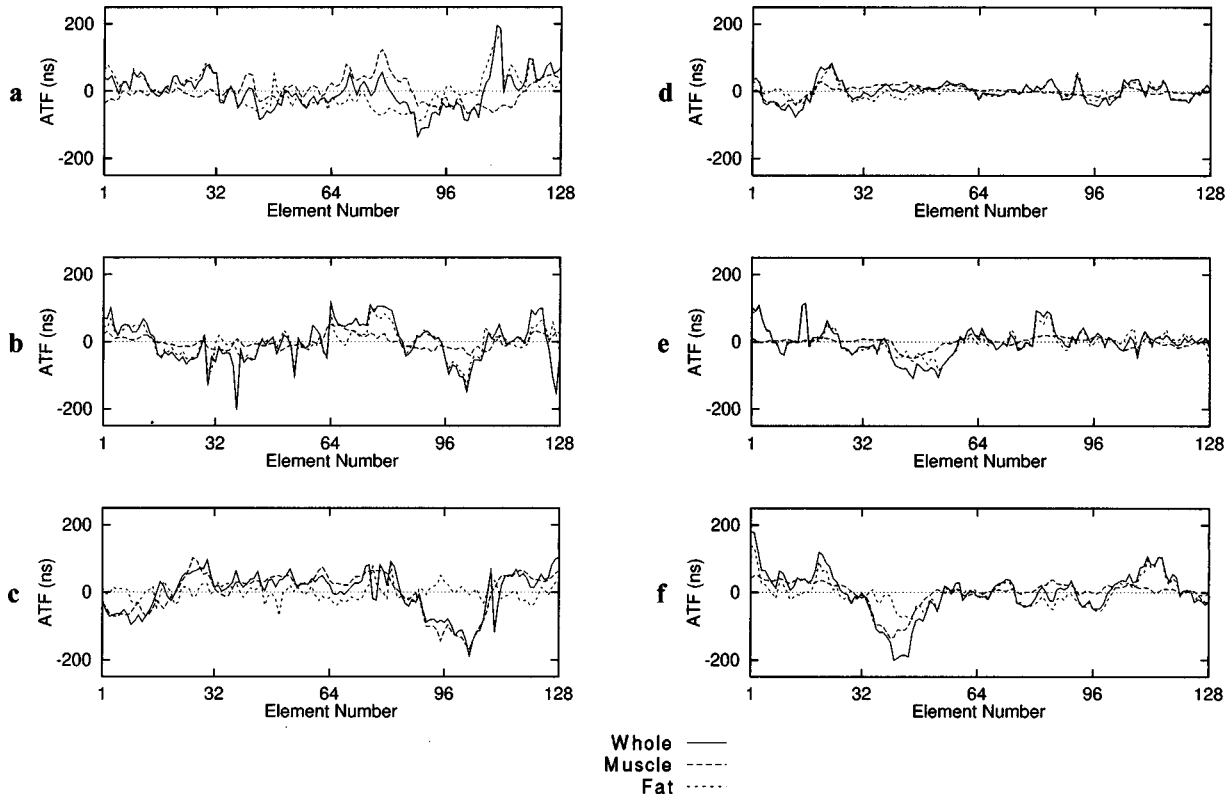

FIG. 4. Arrival time fluctuations (ATF) calculated using the finite-difference, time-domain method for whole specimens, muscle layers, and fat layers. (a) Cross section 75hi. (b) Cross section 77ba. (c) Cross section 87de. (d) Cross section 102gh. (e) Cross section 120de. (f) Cross section 120fe.

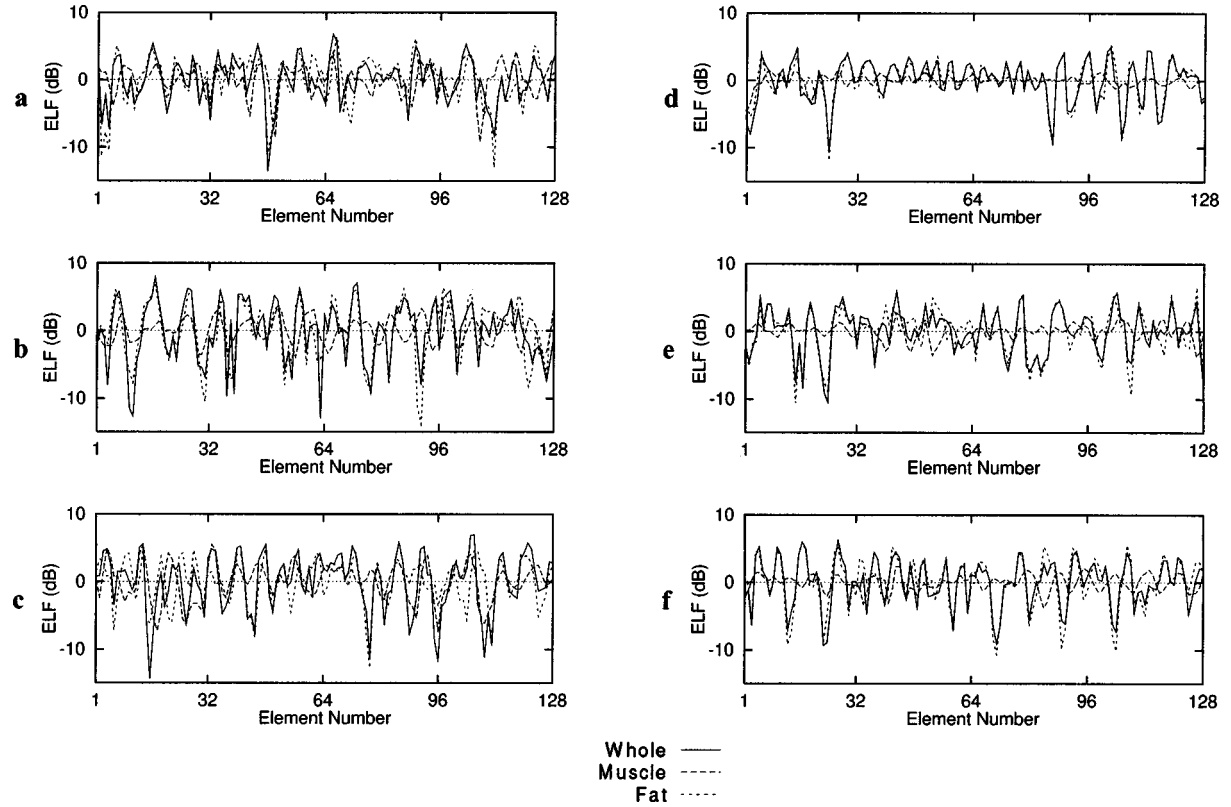

FIG. 5. Energy level fluctuations (ELF) calculated using the finite-difference, time-domain method for whole specimens, muscle layers, and fat layers. (a) Cross section 75hi. (b) Cross section 77ba. (c) Cross section 87de. (d) Cross section 102gh. (e) Cross section 120de. (f) Cross section 120fe.

TABLE II. Wavefront distortion statistics for simulated propagation. Statistics shown include the rms arrival time and energy level fluctuations, correlation lengths (CL) of these fluctuations, and waveform similarity factors for finite-difference, time domain (FDTD) and straight-ray (S-R) simulations employing muscle sections, fat sections and whole specimens.

Specimen	Simulation	Layer	Thickness (mm)	Arrival time fluctuations rms (ns)	Arrival time fluctuations CL (mm)	Energy level fluctuations rms (dB)	Energy level fluctuations CL (mm)	Waveform similarity factor
75hi	FDTD	muscle	9.8	36.5	8.37	2.39	1.60	0.986
		fat	21.3	49.2	8.00	3.45	1.43	0.989
		whole	31.1	53.0	4.70	3.29	1.25	0.957
	S-R	muscle	9.8	38.0	3.55	0.36	5.45	1.000
		fat	21.3	60.6	6.08	0.48	4.79	1.000
		whole	31.1	62.3	2.40	0.42	1.92	1.000
77ba	FDTD	muscle	7.4	19.7	8.59	1.88	1.77	0.996
		fat	17.6	42.5	3.76	4.29	1.61	0.965
		whole	25.0	59.9	4.05	4.44	1.17	0.951
	S-R	muscle	7.4	23.2	2.91	0.35	12.51	1.000
		fat	17.6	51.7	1.52	0.44	2.46	1.000
		whole	25.0	61.6	2.00	0.46	2.09	1.000
87de	FDTD	muscle	12.5	61.3	10.22	2.70	1.97	0.995
		fat	15.9	22.5	1.35	3.26	1.31	0.982
		whole	28.4	60.9	8.68	4.18	1.46	0.948
	S-R	muscle	12.5	62.9	10.54	0.55	13.15	1.000
		fat	15.9	29.7	1.16	0.23	1.18	1.000
		whole	28.4	66.4	6.89	0.60	10.76	1.000
102gh	FDTD	muscle	3.5	15.2	7.99	0.87	1.75	0.999
		fat	15.4	21.6	2.68	2.96	1.31	0.993
		whole	18.9	28.4	3.72	3.10	1.37	0.986
	S-R	muscle	3.5	15.9	7.45	0.24	10.03	1.000
		fat	15.4	26.8	1.73	0.25	2.74	1.000
		whole	18.9	31.9	2.44	0.25	2.83	1.000
120de	FDTD	muscle	9.8	15.2	6.53	1.17	1.77	0.999
		fat	17.8	36.4	2.84	3.37	1.30	0.977
		whole	27.7	43.6	4.88	3.28	1.38	0.980
	S-R	muscle	9.8	16.8	4.63	0.19	8.69	1.000
		fat	17.8	39.8	2.35	0.29	2.58	1.000
		whole	27.7	47.3	3.43	0.38	4.65	1.000
120fe	FDTD	muscle	11.5	38.4	10.32	1.17	1.66	0.999
		fat	17.6	40.2	4.84	3.65	1.45	0.987
		whole	29.1	67.1	8.19	3.41	1.30	0.983
	S-R	muscle	11.5	40.1	10.55	0.42	13.89	1.000
		fat	17.6	45.9	2.13	0.37	2.68	1.000
		whole	29.1	71.3	8.72	0.51	6.11	1.000
Mean	FDTD	muscle	9.1	31.1	8.67	1.70	1.75	0.996
		fat	17.6	35.4	3.91	3.50	1.40	0.982
		whole	26.7	52.2	5.70	3.62	1.32	0.968
	S-R	muscle	9.1	32.8	6.61	0.35	10.62	1.000
		fat	17.6	42.4	2.50	0.34	2.74	1.000
		whole	26.7	56.8	4.31	0.44	4.73	1.000
Standard deviation	FDTD	muscle	3.2	18.1	1.43	0.74	0.13	0.005
		fat	2.1	11.2	2.32	0.45	0.12	0.010
		whole	4.3	14.1	2.16	0.55	0.10	0.017
	S-R	muscle	3.2	18.0	3.42	0.13	3.21	0.000
		fat	2.1	13.0	1.81	0.10	1.16	0.000
		whole	4.3	14.6	2.81	0.12	3.37	0.000

TABLE III. Correlation of finite-difference, time-domain results (FDTD) with straight-ray results (S-R) and with tissue composition.

		Arrival time fluctuations				Energy level fluctuations			
Specimen	Layer	S-R	Muscle	Fat	CT	S-R	Muscle	Fat	CT
	muscle	0.762	0.355	−0.445	−0.241	0.355	−0.074	0.088	−0.141
75hi	fat	0.776	⋯	−0.445	0.738	0.422	⋯	0.349	−0.518
	whole	0.666	0.076	−0.570	0.363	0.363	0.005	0.207	−0.258
	muscle	0.719	0.051	−0.460	0.550	0.353	−0.200	0.365	−0.305
77ba	fat	0.454	⋯	−0.238	0.388	0.518	⋯	0.240	−0.568
	whole	0.501	−0.213	−0.221	0.524	0.572	−0.070	0.246	−0.500
	muscle	0.957	0.896	−0.917	−0.429	0.065	0.022	0.067	−0.261
87de	fat	0.368	⋯	−0.353	0.331	0.617	⋯	0.497	−0.630
	whole	0.783	0.821	−0.821	−0.310	0.190	0.042	0.113	−0.439
	muscle	0.914	0.753	−0.651	−0.290	0.067	0.151	−0.003	−0.402
102gh	fat	0.710	0.433	−0.599	0.590	0.585	−0.282	0.520	−0.644
	whole	0.810	0.426	−0.722	0.250	0.498	0.116	0.274	−0.548
	muscle	0.884	0.794	−0.827	−0.323	0.161	0.072	0.087	−0.355
120de	fat	0.706	⋯	−0.507	0.527	0.471	⋯	0.357	−0.643
	whole	0.787	0.727	−0.620	0.243	0.489	−0.186	0.306	−0.565
	muscle	0.952	0.928	−0.955	−0.597	−0.015	0.054	0.028	−0.259
120fe	fat	0.686	−0.074	−0.653	0.464	0.553	−0.159	0.307	−0.645
	whole	0.872	0.823	−0.842	0.214	0.444	−0.078	0.205	−0.575
	muscle	0.865	0.630	−0.803	−0.222	0.164	0.004	0.013	−0.287
Mean	fat	0.617	⋯	−0.626	0.506	0.528	⋯	0.414	−0.608
	whole	0.737	0.443	−0.782	0.214	0.426	−0.029	0.240	−0.406
	muscle	0.101	0.350	0.215	0.399	0.157	0.124	0.022	0.090
Standard	fat	0.164	⋯	0.038	0.147	0.073	⋯	0.151	0.053
deviation	whole	0.133	0.432	0.085	0.281	0.135	0.106	0.049	0.212

overall distortion, some tissue-specific distortion is seen. For instance, most panels of Fig. 4 show that large-scale arrival time fluctuations from muscle layers and whole abdominal wall cross sections match well. These large-scale time-shift features are generally correlated with positions of large-scale inhomogeneities such as the fatty aponeuroses that occur in cross sections 87de, 120de, and 120fe. Likewise, many large, rapidly varying energy level fluctuations appearing in Fig. 5 are very similar in results for fat layers and whole cross sections, but do not appear in results for muscle layers.

Statistics describing the distortion produced by the six tissue maps using finite-difference simulations are presented in Table II. As with measurements (taken on different specimens) reported in the companion paper,[25] the whole specimens usually cause distortion greater than either of the two component layer distortions and comparable to the geometric sum of the layer distortions. However, in contrast to measurements, the muscle sections usually produce arrival time distortion of lower amplitude (mean rms value 31.1 ns) than the corresponding fat layers (mean 35.4 ns). The rms energy level fluctuations, in agreement with measurements,[25] are substantially greater for fat sections (mean 3.50 dB) than for muscle sections (mean 1.70 dB). Waveform similarity factors for simulations are generally higher (indicating smaller waveform distortion) than those for measured data using the same specimens—the mean waveform similarity factor was 0.968 for finite-difference simulations employing whole cross sections, as opposed to 0.899 for analogous measurements.[23,24]

The straight-ray results reported in Table II show the same trends as those from straight-ray simulations reported in Refs. 23 and 24 using whole abdominal wall cross sections. That is, for each cross section, the rms straight-ray arrival time fluctuation is close to that for the finite-difference computation, so that magnitudes of arrival time fluctuations are predicted fairly well by this simple model. However, the rms energy level fluctuation is considerably less than that for the finite-difference computation, implying that tissue-dependent absorption contributes little to ultrasonic amplitude distortion in the abdominal wall.

Coefficients from correlation of the finite-difference arrival time and energy level fluctuations with the corresponding straight-ray results as well as with the tissue-fraction curves are shown in Table III. In general, finite-difference and straight-ray results correlate more highly for arrival time fluctuations than for energy level fluctuations. This observation is consistent with the differences in fluctuation statistics seen in Table II. The highest mean correlation between finite-difference and straight-ray arrival time fluctuations (0.865) occurs for the muscle sections, implying that phase screen models may be more appropriate for muscle layers than for fat layers. The highest mean correlation between finite-difference and straight-ray energy level fluctuations (0.528) occurs for the fat sections, indicating that amplitude dropouts due to scattering (in the finite-difference simulation) occurred in similar positions to dropouts due to absorption (in the straight-ray simulation). Both effects are associated with connective tissue content because of the high

TABLE IV. Correlation of layer distortion results and summed layer results with whole-specimen results for finite-difference, time-domain (FDTD) and straight-ray (S-R) simulations.

		Whole Specimen			
		FDTD		S-R	
Specimen	Layer	ATF	ELF	ATF	ELF
75hi	Muscle	0.257	0.358	0.347	0.232
	Fat	0.734	0.768	0.809	0.692
	Muscle + Fat	0.942	0.833	1.000	1.000
77ba	Muscle	0.558	0.279	0.571	0.414
	Fat	0.815	0.817	0.932	0.697
	Muscle + Fat	0.826	0.846	0.999	0.999
87de	Muscle	0.890	0.604	0.896	0.926
	Fat	0.048	0.610	0.336	0.359
	Muscle + Fat	0.888	0.870	1.000	1.000
102gh	Muscle	0.652	0.295	0.546	0.495
	Fat	0.828	0.944	0.868	0.510
	Muscle + Fat	0.991	0.977	1.000	1.000
120de	Muscle	0.661	0.133	0.588	0.652
	Fat	0.933	0.914	0.940	0.868
	Muscle + Fat	0.987	0.961	1.000	1.000
120fe	Muscle	0.840	0.094	0.797	0.694
	Fat	0.838	0.899	0.851	0.584
	Muscle + Fat	0.993	0.940	1.000	0.999
Mean	Muscle	0.643	0.294	0.624	0.569
	Fat	0.699	0.825	0.789	0.618
	Muscle + Fat	0.938	0.905	1.000	1.000
Standard deviation	Muscle	0.226	0.182	0.195	0.242
	Fat	0.325	0.124	0.228	0.176
	Muscle + Fat	0.068	0.062	0.000	0.001

acoustic contrast and absorption of connective tissue.

The tissue-fraction correlation coefficients reported in Table III indicate clear relationships between tissue constituents and ultrasonic wavefront distortion components. For the muscle sections, both muscle and fat fractions correlate significantly with arrival time fluctuations (mean correlations 0.630 and −0.803 respectively), while the corresponding coefficient for the connective-tissue fraction (−0.222) does not indicate a significant correlation. (For 128 samples of a random signal, a correlation coefficient with magnitude greater than 0.2875 is significant to a 99.9% confidence level.[30]) Arrival time correlation coefficients are positive for muscle fractions and negative for fat fractions because muscle tissue causes an advance, or positive arrival time fluctuation, in the wavefront, while fat tissue causes a delay, or negative arrival time fluctuation. The large negative correlation (−0.803) between fat content and arrival time fluctuations indicates that fatty inhomogeneities within muscle layers are a major cause of arrival time fluctuations in the abdominal wall. Energy level fluctuations do not correlate well with tissue fractions for the muscle section, although the correlation between energy level fluctuation and connective-tissue fraction is marginally significant (0.287).

For the fat sections, both fat fractions and connective tissue fractions correlate significantly with the arrival time and energy level fluctuations computed by the finite-difference method. The significant negative correlation coefficient (−0.608) between energy level fluctuations and connective tissue fraction indicates that amplitude dropouts occur at positions of high connective tissue content within the subcutaneous fat. Visualization of propagation through cross sections[23] has shown that such dropouts occur when septa scatter energy outside the main direction of propagation. This scattering, which occurs because of the high sound speed and density contrast between connective tissue and fat, is greatest for septa oriented nearly perpendicular to the direction of propagation. Also notable is the effect of a blood vessel (with vessel wall modeled as muscle and connective tissue) in the fat section of cross section 102gh. This vessel causes a significant correlation (0.433) between the muscle fraction and the arrival time fluctuation and a marginal correlation between the muscle fraction and the energy level fluctuation. This large effect of a single blood vessel is similar to that found for a blood vessel in the chest wall in Ref. 6.

Further evidence of the relative contribution of individual layers to wavefront distortion in the abdominal wall is provided by Table IV, which shows correlation coefficients between layer results and whole-specimen results for arrival time and energy level fluctuations. In general, results for both the muscle and fat sections correlate significantly with the whole-specimen results. However, for the finite-difference simulations, the energy level fluctuations for the whole specimen correlate much more highly with those calculated for fat sections (0.825) than with those for muscle sections (0.294). The rows marked ''muscle + fat'' in Table IV refer to correlations between distortion curves for whole cross sections and distortion curves obtained by summing the curves for the corresponding muscle and fat layers. In all cases, the summed section results correlate fairly highly (mean correlation coefficients 0.938 for arrival time fluctuations, 0.905 for energy level fluctuations) with whole-section results for the finite-difference simulations, while the corresponding correlations averaged 1.000 for the straight-ray simulations. Thus, for the finite-difference computations, the wavefront distortion produced by whole cross sections is similar but not equivalent to the sum of distortions caused by their individual layers.

Computed insertion loss values for the whole and layer tissue maps are listed in Table V along with the insertion losses measured for the whole specimens before dissection using the method described in the companion paper.[25] In each case, the loss per unit length is greater for muscle than fat in the straight-ray simulation but greater for fat than muscle in the finite-difference simulation. Since insertion loss effects in the finite-difference simulation were only due to scattering, this observation provides further evidence that fat sections caused more scattering than muscle sections.

In every case shown in Table V, measured insertion losses are greater than insertion losses calculated by either the finite-difference or straight-ray method. However, the measured insertion losses (mean 4.88 dB/cm) agree well with values (mean 4.96 dB/cm) obtained by summing the

TABLE V. Computed and measured insertion loss values. Means and standard deviations of insertion losses are shown for measurements employing whole specimens from which the cross sections were taken as well as straight-ray (S-R) and finite-difference (FDTD) simulations using the cross sections. Also shown is the sum of calculated insertion loss rates for straight-ray and finite-difference simulations (SR + FDTD).

		Measured			S-R			FDTD			
Specimen	Layer	Average (dB)	Standard deviation (dB)	Rate (dB/cm)	Average (dB)	Standard deviation (dB)	Rate (dB/cm)	Average (dB)	Standard deviation (dB)	Rate (dB/cm)	S-R+ FDTD (dB/cm)
	muscle	···	···	···	3.50	0.48	3.57	1.84	2.49	1.88	5.45
75hi	fat	···	···	···	6.27	0.52	2.94	4.25	3.51	2.00	4.94
	whole	14.08	7.66	4.52	9.72	0.67	3.13	5.38	3.30	1.73	4.86
	muscle	···	···	···	2.88	0.36	3.90	1.63	1.91	2.20	6.10
77ba	fat	···	···	···	4.78	0.60	2.71	4.41	4.06	2.51	5.22
	whole	12.87	3.38	5.15	7.61	0.57	3.04	5.69	4.44	2.28	5.32
	muscle	···	···	···	4.77	0.72	3.82	1.32	2.75	1.06	4.88
87de	fat	···	···	···	5.26	0.23	3.31	3.14	3.28	1.97	5.28
	whole	15.68	2.93	5.49	9.99	0.77	3.52	4.14	4.29	1.46	4.98
	muscle	···	···	···	1.41	0.42	4.01	0.60	0.90	1.71	5.72
102gh	fat	···	···	···	4.32	0.27	2.81	3.58	2.99	2.32	5.13
	whole	9.52	4.09	5.04	5.69	0.50	3.01	4.07	3.13	2.15	5.16
	muscle	···	···	···	4.05	0.20	4.12	0.61	1.21	0.62	4.74
120de	fat	···	···	···	4.91	0.31	2.75	3.61	3.42	2.03	4.78
	whole	11.89	3.22	4.22	8.92	0.40	3.22	3.94	3.36	1.42	4.64
	muscle	···	···	···	4.42	0.42	3.85	0.93	1.21	0.81	4.66
120fe	fat	···	···	···	5.08	0.37	2.88	3.98	3.63	2.26	5.14
	whole	11.89	3.22	4.22	9.45	0.51	3.25	4.52	3.37	1.55	4.80
	muscle	···	···	···	3.51	0.43	3.88	1.16	1.75	1.38	5.26
Mean	fat	···	···	···	5.10	0.38	2.90	3.83	3.48	2.18	5.08
	whole	12.81	4.26	4.88	8.56	0.57	3.20	4.62	3.65	1.77	4.96
	muscle	···	···	···	1.23	0.17	0.19	0.52	0.76	0.64	0.59
Standard	fat	···	···	···	0.65	0.15	0.22	0.47	0.36	0.22	0.19
deviation	whole	2.32	1.95	0.51	1.64	0.13	0.19	0.74	0.56	0.37	0.25

insertion losses from the finite-difference computation (due only to scattering effects) and from the straight-ray computation (due only to bulk absorption effects). This result suggests that energy loss from wideband ultrasonic pulses in the abdominal wall may be explained as a combination of bulk absorption effects and scattering effects.

Figures 6 and 7, respectively, show arrival time fluctuations and energy level fluctuations for the finite-difference uniform-layer simulations. For comparison, fluctuation curves for finite-difference simulations with abdominal wall cross sections including full internal structure (identical to the whole-specimen results shown in Figs. 4 and 5) are also shown. Both arrival time and energy level fluctuations are seen to be considerably smaller in the uniform-layer simulations than in the full-structure simulations.

Quantitative results for the simulations employing uniform fat and muscle layers are summarized in Table VI. The mean arrival time fluctuations shown there are less than half those for ''full'' finite-difference and straight-ray simulations that included internal tissue structure (Table II). The correlation lengths of the arrival time fluctuations are much larger than those reported in Table II for the simulations that included full tissue structure. Arrival time fluctuations computed from the finite-difference uniform-layer simulations correlate very well with straight-ray simulations employing the same uniform layers (mean correlation coefficient 0.991), so that time-shift aberration caused in the uniform layer simulations is almost entirely due to large-scale thickness variations rather than refraction at interfaces. These large-scale layer thickness variations, however, do not explain arrival time fluctuations computed from finite-difference simulations employing full tissue structure, because arrival time fluctuations in the uniform layer simulations did not correlate significantly with fluctuations from the full finite-difference simulations (mean correlation coefficient 0.262).

Energy level fluctuations reported for the uniform-layer FDTD simulations provide an indication of the importance of refraction and scattering at tissue interfaces, since other possible causes of energy level fluctuations (i.e., scattering from small structures and tissue-dependent absorption) were absent from these simulations. The energy level fluctuations from the finite-difference uniform-layer simulations are comparable in magnitude to those for the full straight-ray simulations, but much smaller than those observed in the full finite-difference simulations. Energy level fluctuations from the finite-difference uniform-layer simulations did not correlate significantly with energy level fluctuations obtained in either of the simulations employing full tissue structure. Computed waveform similarity factors for all six finite-difference uniform-layer simulations are indistinguishable

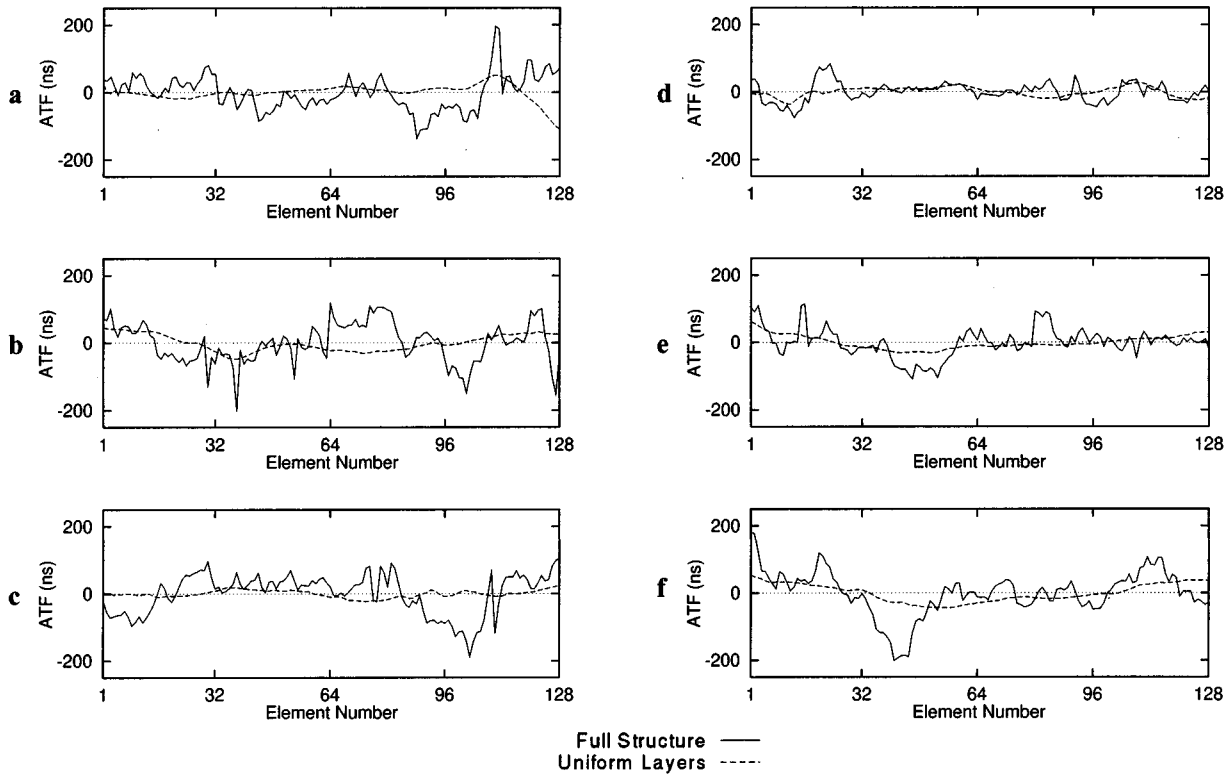

FIG. 6. Arrival time fluctuations (ATF) calculated using the finite-difference, time-domain method for whole specimens with full internal structure and with uniform-tissue fat and muscle layers. (a) Cross section 75hi. (b) Cross section 77ba. (c) Cross section 87de. (d) Cross section 102gh. (e) Cross section 120de. (f) Cross section 120fe.

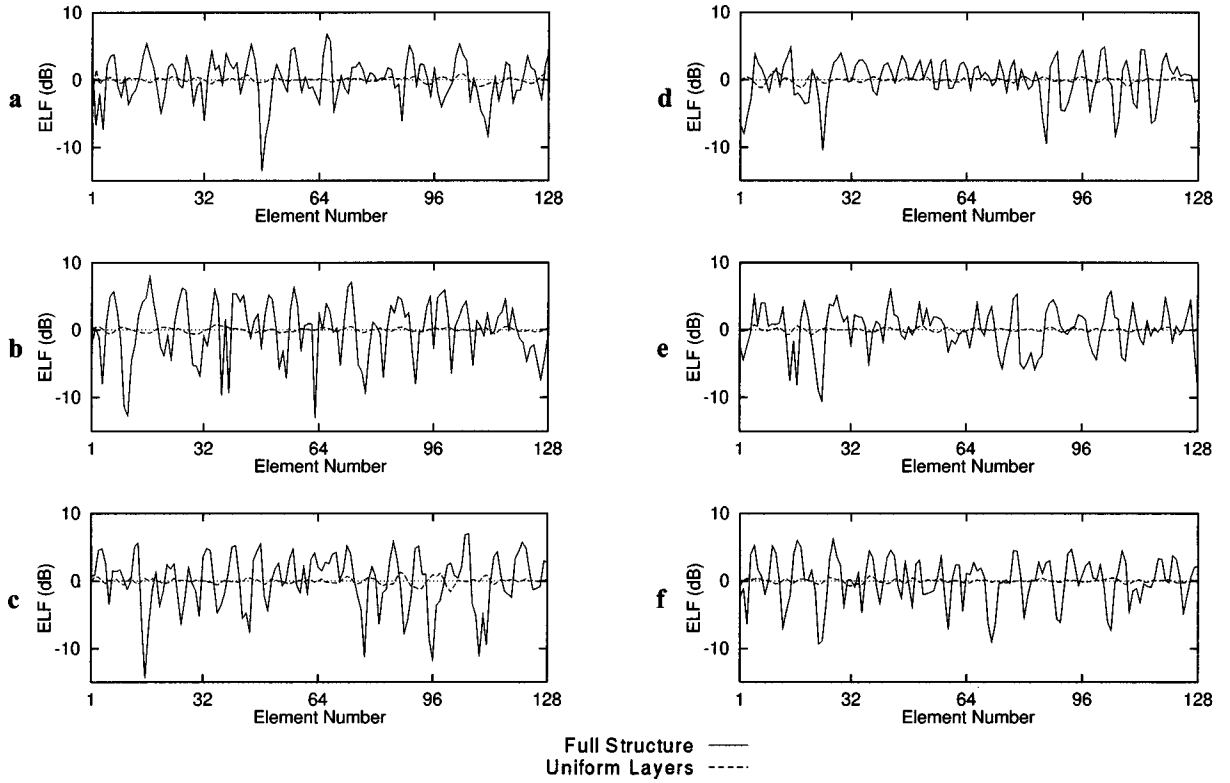

FIG. 7. Energy level fluctuations (ELF) calculated using the finite-difference, time-domain method for whole specimens with full internal structure and with uniform-tissue fat and muscle layers. (a) Cross section 75hi. (b) Cross section 77ba. (c) Cross section 87de. (d) Cross section 102gh. (e) Cross section 120de. (f) Cross section 120fe.

TABLE VI. Wavefront distortion statistics for finite-difference simulation of propagation through uniform fat and muscle layers.

Specimen	Arrival time fluctutations		Energy level fluctuations		Waveform similarity factor	Correlation Coefficient versus S-R (uniform)		Correlation Coefficient versus FDTD (whole)	
	rms (ns)	CL (mm)	rms (dB)	CL (mm)		ATF	ELF	ATF	ELF
75hi	24.2	6.51	0.46	0.97	1.000	0.994	0.183	−0.156	0.086
77ba	24.2	15.01	0.30	2.23	1.000	0.997	0.170	0.145	0.098
87de	10.6	10.88	0.42	1.63	1.000	0.971	0.130	0.064	−0.281
102gh	14.3	9.00	0.39	1.86	1.000	0.991	0.289	0.374	0.020
120de	19.7	16.71	0.27	1.61	1.000	0.996	0.092	0.563	0.146
120fe	26.9	20.33	0.26	1.63	1.000	0.997	0.159	0.581	0.171
Mean	20.0	13.07	0.35	1.66	1.000	0.991	0.171	0.262	0.040
Standard deviation	6.4	5.18	0.08	0.41	0.000	0.010	0.067	0.294	0.166

from unity to four significant figures, indicating that negligible frequency-dependent scattering occurred in these simulations. These small energy level fluctuations, low correlations, and high waveform similarity factors suggest that scattering and refraction at muscle–fat interfaces is not a significant source of amplitude and waveform aberrations observed in ultrasonic propagation through the abdominal wall.

III. DISCUSSION

The results of the simulations reported here provide additional support to the findings reported in the companion measurement paper[25] and add insight regarding the characteristics and causes of ultrasonic wavefront distortion by abdominal wall tissue. As in the measurements,[25] both muscle and fat sections were found to cause substantial wavefront distortion and attenuation. The simulations performed here indicate causes for the different characteristics of distortion produced by each section.

Simulations suggest that muscle sections primarily cause time-shift aberration due to large-scale variations in the amounts of fat, muscle and connective tissue components within muscle layers. In all cases, correlations between finite-difference and straight-ray arrival time fluctuations for the muscle sections were higher than the corresponding correlations for the fat sections, indicating that muscle layers are more appropriately modeled as phase screens than are fat layers. However, arrival time fluctuations for both muscle layers and fat layers had comparable magnitude and correlated significantly with arrival time fluctuations for whole cross sections, so that both layers should be considered important sources of time-shift aberration in transabdominal ultrasonic imaging.

The simulations also suggest that scattering from inhomogeneities within the subcutaneous fat is a major cause of amplitude and waveform distortion in ultrasonic propagation through the abdominal wall. Energy level fluctuations for fat layers were highly correlated with those for whole cross sections, indicating that most amplitude fluctuation features originated in the fat section. High negative correlations between connective-tissue fraction and energy level fluctuations suggest that these amplitude fluctuations are primarily explained by scattering from septa within fatty tissue. This conclusion agrees with qualitative analysis of simulated propagation within abdominal wall cross sections, as reported in Ref. 23. It may also be noted that scattering from septa may become more important for large septa or short ultrasonic wavelengths; in such cases, scattering can cause large fluctuations that are sometimes referred to as diffraction, reflection, or refraction.

The simulations provide insight into the manner in which distortions produced by individual layers combine into distortion produced by whole specimens. For both the simulations presented here and the measurements presented in the companion paper,[25] arrival time fluctuations (ATF) produced by whole specimens are usually comparable to the geometric sum of the fluctuations produced by the individual layers, i.e.,

$$\mathrm{ATF}_{\mathrm{total}} \sim \sqrt{\mathrm{ATF}_{\mathrm{muscle}}^2 + \mathrm{ATF}_{\mathrm{fat}}^2}\,.$$

For arrival time fluctuations measured in Ref. 25 as well as those simulated here by finite-difference and straight-ray methods, the geometric sum of the rms fluctuations caused by individual layers is within 30% of the rms fluctuation for whole specimens. Since fluctuations caused by two independent random processes should add geometrically, this result suggests that distortion produced by fat layers is roughly independent of that produced by muscle layers, and that both layers can approximately be considered random aberrators. However, some anomalous results appear in both measurements and simulations; in some cases, the rms arrival time or energy level fluctuation for a whole specimen is less than the rms fluctuation for one or both of the individual layers.

Such differences are possible because, in the case of the whole specimen, the wavefront impinging on the fat layer has already been distorted by propagation through the muscle layer. If the distortion-producing features of the muscle and fat layers are not truly independent of each other, the aberrated wavefront may interact with the structures in the fat layer in ways that reduce or exaggerate the overall distortion level. For instance, Fig. 4(c) shows that near the center of cross section 87de, large-scale arrival time fluctuations occurring in the fat layer partially cancel those that arise in the muscle layer. This occurs in part because, as can be seen in Fig. 1, the fat layer is thicker (causing a large-scale delay in the wavefront) in this region of the cross sec-

tion where the muscle layer contains little fat (causing a relative advance in the wavefront). Because of the importance of large-scale, ordered structure in causing cumulative effects such as this, it may be noted that the human abdominal wall is not fully represented by simple random-process models. In general, the manner in which distortions caused by individual layers combine will be influenced by the specific structure of the tissue being studied.

Results for the insertion loss, or the attenuation in the wavefront amplitude, have shown that both scattering effects (as modeled in finite-difference simulations) and absorption effects (as modeled in straight-ray simulations) make significant contributions to the total insertion loss. Insertion losses estimated by summing results from these two simulations agree well with measured insertion losses for the same specimens. This result suggests that procedures for estimating attenuation by the human abdominal wall, whether for correction of amplitude aberration or quantitative estimation of scattering properties, should consider scattering effects as well as absorption effects. Relative contributions of absorption and scattering to total attenuation, however, can be different in tissues having structure different from the abdominal wall. For instance, some experimental results have suggested that scattering accounts for 2%–18% of attenuation in liver tissue for frequencies between 1.2 MHz and 7 MHz,[31,32] while the current experimental and simulated results suggest that scattering accounts for about 36% of total insertion loss in the human abdominal wall for pulses centered at 3.75 MHz. This discrepancy is likely associated with differences in morphology between human abdominal wall and liver tissue.

Simulations performed using straight-ray and uniform-layer approximations allow comparison of the present tissue model to others previously employed in medical ultrasound. The straight-ray simulation method is analogous to modeling the abdominal wall as a single phase and amplitude screen at the receiving aperture. Previous results[23,24] have shown that this model incompletely describes wavefront distortion from the human abdominal wall. The current study, while confirming this conclusion, also indicates that single-phase-screen models describe distortion produced by muscle layers more accurately than distortion produced by fat layers. This result suggests that aberration correction techniques employing single-phase-screen models may provide greater gains when wavefront distortion is due to thick muscle layers than when distortion is associated with obesity.

Others have modeled human tissue as a series of layers of nominally homogeneous properties. Such uniform layers can cause ultrasonic aberration either by variations in thickness[7,8,33] or by refraction and scattering at interfaces between layers.[4,15,34,35] The uniform-layer FDTD simulations performed in the present study provide a test of the appropriateness of these models. Arrival time fluctuations from uniform-layer simulations were considerably smaller than those for simulations including full internal structure and were also uncorrelated with full-structure simulations, so that thickness variations of nominally uniform layers appear to be a minor cause of wavefront distortion. The small energy level fluctuations and high waveform similarity factors computed for uniform-layer simulations suggest that refraction and scattering at muscle–fat interfaces is not a significant source of wavefront distortion observed in the abdominal wall. Since comparable sound-speed and impedance mismatches occur between other tissue layers such as skin and fat, the present results suggest that scattering from internal tissue structures contributes more strongly to observed wavefront distortion than do refraction and scattering from any interfaces between tissue layers. Thus, although models assuming uniform tissue layers have successfully corrected image artifacts associated with refraction caused by specific anatomic features,[34,36] such models may not provide optimal correction for focus degradation in transabdominal ultrasonic imaging.

A third model sometimes used in simulation studies of ultrasonic imaging includes single or multiple phase screens synthesized using measured or estimated aberration statistics. Typically, a few parameters such as rms distortion values and correlation lengths are employed as parameters for realization of a simple random distribution.[13,15,37,38] These models, by design, produce distortion that is statistically similar to aberration caused by tissues. However, tissue-specific features of ultrasonic wavefront distortion are not depicted by simple stochastic models because tissue is not a true random medium. The ordered, anisotropic distortion induced by muscle fibers is one example of a distortion feature important to ultrasonic imaging that is not accounted for by simple random aberrator models. Another example is the distortion caused by septa aligned close to the propagation direction within the subcutaneous fat, including scattering and arrival-time variations that increase cumulatively with propagation through the fat layer. Because tissue structure determines the wavefront distortion encountered in clinical practice, statistical representations of tissue are also of little use for distortion correction methods. Since tissue structure on scales important to medical ultrasound ($\sim 1-20$ mm) varies widely among individuals, effective aberration correction will require compensation specific to each patient and view.

Worthy of comment are differences between the specimens employed here for tissue-type mapping and those used in Ref. 25 for two-dimensional wavefront distortion measurements of whole specimens and individual sections. The relative thicknesses of the specimens employed were comparable, having a mean of 26.6 mm for the mapped specimens, and a mean of 24.4 mm for the measured specimens. However, the muscle layer was usually about half the thickness of the fat layer for the mapped specimens, while muscle layer thicknesses were typically close to fat layer thicknesses for the measured specimens. The muscle layer was actually thicker than the fat layer for one specimen (118) measured in Ref. 25.

The discrepancy in muscle thickness between the two specimen groups may partially explain the relatively low distortion values found for simulated propagation through muscle sections in the present paper. Another possible reason for the low distortion associated with muscle sections in the present paper may be the result of inaccuracies in tissue mapping. In particular, the fibrous microstructure of muscle was not mapped in the present study, and some connective tissue

occurring in the muscle layers was not accurately mapped, since the staining technique employed provided less contrast between muscle and connective tissue than between fat and connective tissue. Finally, another likely cause of disagreement between the simulations reported here and the measurements reported in Ref. 25 is that the present simulations were performed in two dimensions. Further discussion of this limitation is given in Ref. 23.

The absence of frequency-dependent absorption is a possible source of error in estimates of total tissue attenuation and energy level fluctuations from the straight-ray computations. However, since absorption in tissue increases approximately linearly with frequency, lower absorption for frequency components below the pulse center frequency would nearly cancel higher absorption for frequency components above the center frequency. For this reason, the neglect of frequency-dependent absorption is not considered to be a significant source of error in the attenuation or energy level fluctuation curves computed using the straight-ray method. Still, inclusion of frequency-dependent absorption could result in some waveform distortion effects. Therefore, if actual waveforms were employed in this simulation, the peak-to-peak insertion losses could deviate from the bulk absorption calculated above and waveform similarity factors could deviate from unity even in the absence of scattering.

Likewise, the absence of any tissue-specific absorption from the finite-difference computations is a possible source of inaccuracy when using the present finite-difference method to estimate waveform and energy level distortion. Because frequency-dependent absorption would cause additional waveform distortion, the absence of frequency-dependent absorption may be a partial explanation for the large waveform similarity factors computed from simulated wavefronts. However, since energy level fluctuations obtained from the straight-ray simulation using tissue-dependent absorption are much smaller than energy level fluctuations from the finite-difference simulations, inclusion of absorption in the finite-difference simulations would have only a small effect on the computed energy level distortion.

More detailed discussion of limitations and sources of error for the simulation methods employed is given in Ref. 23.

IV. CONCLUSIONS

Simulation results have been presented to provide quantifiable correlation between tissue morphology and ultrasonic wavefront distortion produced by the human abdominal wall.

The results support conclusions based on measurements[25] that used whole abdominal specimens and their individual fat and muscle layers. Specifically, the finite-difference simulation results show that both fat and muscle layers cause significant distortion. Correlation of distortion curves with tissue composition indicates that inhomogeneous regions such as fatty inclusions within muscle layers cause significant arrival time fluctuations, while amplitude aberration is predominantly caused by scattering from septa within the subcutaneous fat. One difference between the finite-difference and measurement results is that although muscle layers produced more arrival time variation in the measurements, comparable arrival time fluctuation was caused by muscle and fat layers in the simulations. However, in both cases, fat layers caused greater energy level distortion.

Additional simulations performed using a straight-ray model suggest that phase-screen models are more appropriate for muscle layers of the abdominal wall than for the subcutaneous fat, but that single phase-screen models incompletely describe aberration caused by the human abdominal wall. Simulations performed using a uniform-layer model indicate that refraction at interfaces between tissue layers, as well as varying thickness of muscle and fat sections of the abdominal wall, are minor sources of ultrasonic wavefront distortion compared to large-scale inhomogeneities and effects caused by internal structure. The importance of specific ordered tissue structures to cumulative distortion effects within layers, as well as to the combination of wavefront distortion by fat and muscle layers, suggests that tissue models employing simple random processes incompletely depict wavefront distortion caused by the abdominal wall.

In summary, these results suggest that models of ultrasonic propagation within human soft tissues, whether employed within aberration correction algorithms or imaging simulations, should include realistic depictions of tissue morphology to obtain accurate results. Models of tissue morphology for aberration correction should also accurately depict tissue structures specific to the individual and location of interest.

ACKNOWLEDGMENTS

The authors thank Dr. Leon A. Metlay for advice during construction of the tissue maps and for other consultation regarding abdominal wall morphology. Dong-Lai Liu is thanked for providing the original two-dimensional version of the distortion estimation code. Funding for this investigation was provided by the University of Rochester Diagnostic Ultrasound Research Laboratory Industrial Associates, NIH Grants DK 45533, HL 50855, and CA 74050, and US Army Grant DAMD-17-94-J-4384. Computations were performed at the Cornell National Supercomputing Facility, which was supported in part by the National Science Foundation, New York State, and the IBM Corporation, and at the Center for Academic Computing of the Pennsylvania State University.

[1] Y. Sumino and R. C. Waag, ''Measurements of ultrasonic pulse arrival time differences produced by abdominal wall specimens,'' J. Acoust. Soc. Am. **90**, 2924–2930 (1991).
[2] L. M. Hinkelman, D.-L. Liu, L. A. Metlay, and R. C. Waag, ''Measurements of ultrasonic pulse arrival time and energy level variations produced by propagation through abdominal wall,'' J. Acoust. Soc. Am. **95**, 530–541 (1994).
[3] P. D. Freiburger, D. C. Sullivan, B. H. LeBlanc, S. W. Smith, and G. E. Trahey, ''Two dimensional ultrasonic beam distortion in the breast: In-vivo measurements and effects,'' Ultrason. Imaging **14**(4), 398–414 (1992).
[4] Q. Zhu and B. D. Steinberg, ''Large-transducer measurements of wavefront distortion in the female breast,'' Ultrason. Imaging **14**(3), 276–299 (1992).
[5] L. M. Hinkelman, D.-L. Liu, R. C. Waag, Q. Zhu, and B. D. Steinberg, ''Measurement and correction of ultrasonic pulse distortion produced by the human breast,'' J. Acoust. Soc. Am. **97**, 1958–1969 (1995).
[6] L. M. Hinkelman, T. L. Szabo, and R. C. Waag, ''Measurements of ul-

trasonic pulse distortion produced by the human chest wall,'' J. Acoust. Soc. Am. **101**, 2365–2373 (1997).
[7] M. O'Donnell and S. W. Flax, ''Phase-aberration correction using signals from point reflectors and diffuse scatterers: Measurements,'' IEEE Trans. Ultrason. Ferroelectr. Freq. Control **35**(6), 768–774 (1988).
[8] L. Nock, G. E. Trahey, and S. W. Smith, ''Phase aberration correction in medical ultrasound using speckle brightness as a quality factor,'' J. Acoust. Soc. Am. **85**, 1819–1833 (1989).
[9] D. Rachlin, ''Direct estimation of aberrating delays in pulse-echo imaging systems,'' J. Acoust. Soc. Am. **88**, 191–198 (1990).
[10] D.-L. Liu and R. C. Waag, ''Time-shift compensation of ultrasonic pulse focus degradation using least-mean-square error estimates of arrival time,'' J. Acoust. Soc. Am. **95**, 542–555 (1994).
[11] M. O'Donnell and S. W. Flax, ''Phase aberration measurements in medical ultrasound: Human studies,'' Ultrason. Imaging **10**(1), 1–11 (1988).
[12] B. S. Robinson, A. Shmulewitz, and T. M. Burke, ''Waveform aberrations in an animal model,'' 1994 IEEE Ultrason. Symp. Proc. **3**, 1619–1624 (1994).
[13] D.-L. Liu and R. C. Waag, ''Correction of ultrasonic wavefront distortion using backpropagation and a reference waveform method for time-shift compensation,'' J. Acoust. Soc. Am. **96**, 649–660 (1994).
[14] C. Dorme and M. Fink, ''Ultrasonic beam steering through inhomogeneous layers with a time reversal mirror,'' IEEE Trans. Ultrason. Ferroelectr. Freq. Control **43**(1), 167–175 (1996).
[15] A. P. Berkhoff and J. M. Thijssen, ''Correction of concentrated and distributed aberrations in medical ultrasound imaging,'' 1996 IEEE Ultrasonics Symp. Proc. **2**, 1405–1410 (1996).
[16] S. Krishnan, P.-C. Li, and M. O'Donnell, ''Adaptive compensation for phase and magnitude aberrations,'' IEEE Trans. Ultrason. Ferroelectr. Freq. Control **43**(1), 44–55 (1996).
[17] Q. Zhu and B. D. Steinberg, ''Deabberation of incoherent wavefront distortion: an approach toward inverse filtering,'' IEEE Trans. Ultrason. Ferroelectr. Freq. Control **44**(3), 575–589 (1997).
[18] R. C. Waag, D. Dalecki, and W. A. Smith, ''Estimates of wave front distortion from measurements of scattering by model random media and calf liver,'' J. Acoust. Soc. Am. **85**, 406–415 (1989).
[19] L. A. Ødegaard, ''Phase Aberration Correction in Medical Ultrasound Imaging,'' Ph.D. thesis, University of Trondheim, Trondheim, Sweden, 1995.
[20] L. Ødegaard, E. Halvorsen, B. Ystad, H. G. Torp, and B. Angelsen, ''Delay and amplitude focusing through the body wall; A simulation study,'' 1996 IEEE Ultrason. Symp. Proc. **2**, 1411–1414 (1996).
[21] C. W. Manry, Jr., and S. L. Broschat, ''FDTD simulations for ultrasound propagation in a 2-D breast model,'' Ultrason. Imaging **18**(1), 25–34 (1996).
[22] A. P. Berkhoff, P. M. van den Berg, and J. M. Thijssen, ''Simulation of wave propagation through aberrating layers of biological media,'' 1994 IEEE Ultrason. Symp. Proc. **3**, 1797–1800 (1994).
[23] T. D. Mast, L. M. Hinkelman, M. J. Orr, V. W. Sparrow, and R. C. Waag, ''Simulation of ultrasonic pulse propagation through the abdominal wall,'' J. Acoust. Soc. Am. **102**, 1177–1190 (1998).
[24] T. D. Mast, L. M. Hinkelman, M. J. Orr, V. W. Sparrow, and R. C. Waag, ''Erratum: 'Simulation of ultrasonic pulse propagation through the abdominal wall' [J. Acoust. Soc. Am. **102**, 1177–1190 (1997)],'' J. Acoust. Soc. Am. **104**, 1124–1125 (1998).
[25] L. M. Hinkelman, T. D. Mast, L. A. Metlay, and R. C. Waag, ''The effect of abdominal wall morphology on ultrasonic pulse distortion. Part I. Measurements,'' J. Acoust. Soc. Am. **104**, 3635–3649 (1998).
[26] L. M. Hinkelman, L. A. Metlay, C. J. Churukian, and R. C. Waag, ''Modified Gomori trichrome stain for macroscopic tissue slices,'' J. Histotech. **19**(4), 321–323 (1996).
[27] R. Warwick and P. L. Williams (eds.), *Gray's Anatomy* (Saunders, Philadelphia, 1973), 35th ed., pp. 488–490, 519–527.
[28] H. Gray, *Gray's Anatomy*, edited by T. P. Pick and R. Howden (Gramercy, New York, 1977), pp. 358–364 (facsimile of 1901 American edition of *Anatomy, Descriptive and Surgical*).
[29] J. L. Matthews and J. H. Martin, *Atlas of Human Histology and Ultrastructure* (Lea & Febiger, Philadelphia, 1971), pp. 54–55, 102–119.
[30] P. R. Bevington, *Data Reduction and Error Analysis for the Physical Sciences* (McGraw–Hill, New York, 1969), pp. 310–311.
[31] K. J. Parker, ''Ultrasonic attenuation and absorption in liver tissue,'' Ultrasound Med. Biol. **9**, 363–369 (1983).
[32] J. A. Campbell, ''Measurements of ultrasonic differential and total scattering cross sections for tissue characterization,'' Ph. D. thesis, University of Rochester, Rochester, New York, 1984.
[33] H. Wang, E. S. Ebbini, M. O'Donnell, and C. A. Cain, ''Phase aberration correction and motion correction for ultrasonic hyperthermia phased arrays: experimental results,'' IEEE Trans. Ultrason. Ferroelectr. Freq. Control **41**(1), 34–43 (1994).
[34] G. Kossoff, D. A. Carpenter, D. E. Robinson, D. Ostry, and P. L. Ho, ''A sonographic technique to reduce beam distortion by curved interfaces,'' Ultrasound Med. Biol. **15**(4), 375–382 (1989).
[35] L. A. Ledoux, A. P. Berkhoff, and J. M. Thijssen, ''Ultrasonic wave propagation through aberrating layers: experimental verification of the conjugate gradient Rayleigh method,'' IEEE Trans. Ultrason. Ferroelectr. Freq. Control **43(1)**, 158–166 (1996).
[36] D. A. Carpenter, G. Kossoff, and K. A. Griffiths, ''Correction of distortion in US images caused by subcutaneous tissues: results in tissue phantoms and human subjects,'' Radiology **195**, 563–567 (1995).
[37] L. A. Ødegaard, ''Using signals scattered from diffuse inhomogeneities to correct for phase aberrations caused by a phase-screen far from the transducer,'' 1995 IEEE Ultrason. Symp. Proc. **2**, 1443–1447 (1995).
[38] W. E. Walker and G. E. Trahey, ''Aberrator integration error in adaptive imaging,'' IEEE Trans. Ultrason. Ferroelectr. Freq. Control **44**(4), 780–791 (1997).